Concentration of H, Si, Cl, K, Fe, and Th in the low- and mid-latitude regions of Mars

W. V. Boynton,[1] G. J. Taylor,[2] L. G. Evans,[3] R. C. Reedy,[4] R. Starr,[5] D. M. Janes,[1]
K. E. Kerry,[1] D. M. Drake,[6] K. J. Kim,[1,4] R. M. S. Williams,[1] M. K. Crombie,[1]
J. M. Dohm,[7] V. Baker,[7] A. E. Metzger,[8] S. Karunatillake,[9] J. M. Keller,[1,10]
H. E. Newsom,[4] J. R. Arnold,[11] J. Brückner,[12] P. A. J. Englert,[2] O. Gasnault,[13]
A. L. Sprague,[1] I. Mitrofanov,[14] S. W. Squyres,[9] J. I. Trombka,[15] L. d'Uston,[13]
H. Wänke,[12] and D. K. Hamara[1]

[1]   We report maps of the concentrations of H, Si, Cl, K, Fe, and Th as determined by the Gamma Ray Spectrometer (GRS) on board the 2001 Mars Odyssey Mission for $\pm\sim45°$ latitudes. The procedures by which the spectra are processed to yield quantitative concentrations are described in detail. The concentrations of elements determined over the locations of the various Mars landers generally agree well with the lander values except for Fe, although the mean of the GRS Fe data agrees well with that of Martian meteorites. The water-equivalent concentration of hydrogen by mass varies from about 1.5% to 7.5% (by mass) with the most enriched areas being near Apollinaris Patera and Arabia Terra. Cl shows a distribution similar to H over the surface except that the Cl content over Medusae Fossae is much greater than elsewhere. The map of Fe shows enrichment in the northern lowlands versus the southern highlands. Silicon shows only very modest variation over the surface with mass fractions ranging from 19% to 22% over most of the planet, though a significant depletion in Si is noted in a region west of Tharsis Montes and Olympus Mons where the Si content is as low as 18%. K and Th show a very similar pattern with depletions associated with young volcanic deposits and enrichments associated with the TES Surface Type-2 material. It is noted that there appears to be no evidence of significant globally distributed thick dust deposits of uniform composition.

1. Introduction

[2]   One of the basic keys to an understanding of the formation and evolution of Mars is knowledge of the elemental composition of its surface. In the past, there have been several studies carried out to determine the surface composition of Mars, either globally or at specific locations on the planet. These have included Earth-based observational programs using reflectance spectroscopy [e.g., *Singer et al.*, 1979; *Merényi et al.*, 1996a, 19996b], and more recently, orbital studies at regional to global scales carried out using visible and infrared imaging [e.g., *Bandfield et al.*, 2000; *Christensen et al.*, 2001; *Bandfield*, 2002; *Bibring et al.*, 2005; *Gendrin et al.*, 2005]. Lander missions have yielded more detailed elemental (and mineralogical) information at a few locations on the Martian surface, including

[1]Lunar and Planetary Laboratory, University of Arizona, Tucson, Arizona, USA.

[2]Institute of Geophysics and Planetology, University of Hawaii at Manoa, Honolulu, Hawaii, USA.

[3]Science Programs, Computer Sciences Corporation, Lanham, Maryland, USA.

[4]Institute of Meteoritics, University of New Mexico, Albuquerque, New Mexico, USA.

[5]Department of Physics, Catholic University of America, Washington, D. C., USA.

[6]TechSource, Santa Fe, New Mexico, USA.

[7]Department of Hydrology and Water Resources, University of Arizona, Tucson, Arizona, USA.

[8]Jet Propulsion Laboratory, California Institute of Technology, Pasadena, California, USA.

[9]Center for Radiophysics and Space Research, Cornell University, Ithaca, New York, USA.

[10]Now at Physics Department, California Polytechnic State University, San Luis Obispo, San Luis Obispo, California, USA.

[11]Department of Chemistry, University of California, San Diego, La Jolla, California, USA.

[12]Max-Planck-Institut für Chemie, Mainz, Germany.

[13]Centre d'Etude Spatiale des Rayonnements, CNRS/UPS, Toulouse, France.

[14]Space Research Institute (IKI), Moscow, Russia.

[15]NASA Goddard Space Flight Center, Greenbelt, Maryland, USA.

Viking 1 and 2 [*Clark et al.*, 1977; *Baird et al.*, 1977; *Toulmin et al.*, 1977], Pathfinder [*Bell et al.*, 2000; *Wänke et al.*, 2001] and the Mars Exploration Rovers (MER), both on Meridiani Planum [*Rieder et al.*, 2004; *Clark et al.*, 2005] and in Gusev Crater [*Gellert et al.*, 2004; *McSween et al.*, 2004; *Gellert et al.*, 2006]. In addition, analyses of meteorites of Martian provenance provide highly detailed compositional information that can be compared to lander in situ measurements [*Morris et al.*, 2000]. These studies, however, have either been spatially incomplete (with less than global coverage and only a few microns penetration depth) or have provided data on only a few minerals.

[3] Gamma-ray detectors have been successfully used from orbit around the Moon [*Bielefeld et al.*, 1976; *Davis*, 1980; *Lawrence et al.*, 1998] and around the asteroid Eros [*Trombka et al.*, 2000]. Advances in gamma-ray detectors since the Apollo days have increased their sensitivity to a number of elements. Their use in orbit around Mars [*Boynton et al.*, 1992, 2004; *Surkov et al.*, 1993] offers a unique opportunity to apply this technique to a planet with an atmosphere thin enough to allow detection of gamma rays produced in the near-surface rock and soil materials (referred to here as regolith) but thick enough to serve as a collimator allowing slightly better spatial resolution. The Gamma Ray Spectrometer (GRS) on the 2001 Mars Odyssey Mission uses a solid-state Ge detector, which has significantly better spectral resolution than the scintillation detectors used on the prior missions.

[4] The Gamma Subsystem (GS) is part of a suite of instruments [*Boynton et al.*, 2004] designed to detect a wide range of gamma-ray energies and energetic particles emanating from the surface of Mars and from cosmic rays. These instruments include the High Energy Neutron Detector (HEND), the Neutron Spectrometer (NS), and the GS. The three instruments of the GRS are designed to work synergistically to investigate the composition and nature of the Martian regolith. Analysis of the data acquired from the GRS instrument suite has already shown the presence of significant subsurface ice deposits in regions poleward of approximately 60° north and 60° south latitudes [*Boynton et al.*, 2002; *Feldman et al.*, 2002; *Mitrofanov et al.*, 2002; *Litvak et al.*, 2006] and has mapped the distribution of H in low and mid latitudes as well [*Feldman et al.*, 2004, 2005; *Mitrofanov et al.*, 2004; *Fialips et al.*, 2005].

[5] The gamma rays measured by the Mars Odyssey GRS are made mainly by two processes, the decay of long-lived, naturally occurring radioactive elements (the isotope ^{40}K and the elements U and Th with their daughter isotopes) and by the interactions of cosmic ray particles. Most cosmic ray–produced gamma rays used to determine elemental abundances are made by the scattering of fast (energies of $\sim$1–20 MeV) neutrons from a nucleus or by the capture of neutrons at or near thermal ($\sim$0.02 eV) energies. The gamma rays measured are made in the top few tens of centimeters of the surface. The use of gamma rays to determine the composition of a planetary body is reviewed by *Evans et al.* [1993] and references therein. Gamma-ray spectrometry at Mars is complicated by the Martian atmosphere, variable amounts of water in the surface, variations in the size and composition of rocks, and compositional variations with depth [cf. *Evans and Squyres*, 1987; *Masarik and Reedy*, 1996; *Squyres and Evans*, 1992]. The

amount of any dust or water in the atmosphere is much too thin to produce a detectable flux of gamma rays. A few gamma-ray spectra were measured by Soviet spacecraft at Mars, but the spectral and spatial resolutions were poor [e.g., *Trombka et al.*, 1992; *d'Uston et al.*, 1989].

[6] The 2001 Mars Odyssey Mission entered Mars orbit on 24 October 2001, and the orbit was circularized through aerobraking over the ensuing 3 months [*Saunders et al.*, 2004]. The spacecraft entered final mapping orbit on 19 February 2002. The Gamma Subsystem (GS) was turned on, and the GS detector was annealed by heating to remove the effects of damage caused by cosmic ray exposure. After anneal and before the boom holding the GS was deployed from the spacecraft, some data were gathered in order to check out the system operation. These data also showed that the Martian surface had high H_2O contents [*Boynton et al.*, 2002], but they are not included in this work. The boom was deployed on 3 June 2002, and data collection began on 8 June of that year. Data gathering has been continuous since that time except for periods when the spacecraft entered safemode. (In safemode, the spacecraft changes its orientation such that the passive-radiative cooler on the GS detector looses its clear view of space and the GS detector warms. Warming of the detector activates the effect of the accumulated radiation dose received since the last annealing, and thus the detector again requires annealing [*Boynton et al.*, 2004]. The safemode anneal cycles typically take about 28 days before data acquisition can resume.) In addition, data collected during Solar Particle Events (SPEs) and intense solar X-ray flares are not included in the data reported here. Data reported here and in the other GRS manuscripts in this issue include data collected from 8 June 2002, up to the start of a long safemode period on 2 April 2005.

[7] As an illustration of the rich data set available from the GS part of the GRS instrument suite, this work presents concentration maps which have been made available at this state of the data processing for the elements: H, Si, Cl, K, Fe and Th. In this paper, we will describe the data acquisition and processing procedures used by the GS, and present the results for the global distribution of these six elements of geologic interest.

2. Data Processing
2.1. Collection and Processing of Gamma-Ray Spectra

[8] Since the basis of the gamma-ray spectrometry technique for determination of elemental concentrations has been discussed in detail by *Boynton et al.* [2004], only an overview will be given here. The concentrations for all elements were assumed to be homogeneous in the top $\sim$1 meter of the surface. For two of the elements discussed in this work, K and Th, the intensities of their gamma rays at the surface are proportional to the amount of element present times their decay constants. The concentration of Si is determined via a gamma ray emitted from a nuclear excited state that is populated by interactions with high-energy (fast) neutrons. In this case, the emission rate is proportional to the flux of fast neutrons in the near surface, the interaction cross section, and the amount of silicon present. The concentrations of the remaining elements presented here, H, Cl, and Fe, are determined from prompt

Table 1. Gamma Rays Used in the Analyses in This Work, the Radius of the Circle on the Planet From Which Half of the Signal Comes, the Depth Beneath the Surface From Which Half the Signal Originates, the Fraction of the Signal Due to Background Lines for the Entire Analyzed Region Between ±45° Latitude, the Size of the Grid on Which the Data Were Summed, and the Radius of the Circle Used to Smooth the Data for the Maps[a]

	Gamma Rays, keV	50%-Signal Radius		Background Correction, %	Grid Size, deg	Smoothing Radius, deg
		km	deg			
Si	1778.97	219	3.7	11	2 × 2	15
Fe	7127(d,e), 7638(d)	267	4.5	0	2 × 2	10
H	2223.25	222	3.8	29	5 × 5	10
Cl	1951.14, 1959.35	217	3.7	0	5 × 5	10
	5599.84(e), 6110.84	260	4.4	0	5 × 5	10
	7790.33	270	4.6	0	5 × 5	10
K	1460.82	215	3.6	33	2 × 2	5
Th	2614.53	240	4.1	21	2 × 2	10

   [a]Here (d) is a doublet of two lines of similar energy and (e) is an escape line formed when 511.00 keV are lost from the detector after positron annihilation in the detector.

gamma rays emitted following the capture of low-energy (thermal) neutrons. Their gamma-ray emission rates are proportional to the flux of thermal neutrons times the capture cross section along with the amount of the element present.

[9] The gamma-ray detection system has no collimation or focusing system, so gamma rays from all directions are recorded. About 50% of the gamma rays from the surface come from within a radius of 240 km (4° of arc) from nadir [*Boynton et al.*, 2004]. The 50%-signal GS footprint varies as a function of both the method of production and energy of the gamma ray (Table 1). Similarly the depth in the surface above which 50% of the signal originates is also dependent on the same parameters and is given in Table 1. Note that depth is given in units of column density (g/cm^2) since that is the parameter that relates to both neutron flux and gamma-ray attenuation.

[10] Gamma-ray spectra are collected at a rate of 360 spectra per orbit, for a duration of about 19.75 s each. Each spectrum consists of 16,384 channels of discrete counts spanning the energy range from 0 to 10 MeV. The spectra are stored in a large database from which they are subsequently retrieved for a particular region and/or time period of interest, summed together to increase the statistical precision, and processed to determine the intensity of the emission lines in the resultant spectra [*Evans et al.*, 2006]. Before the individual spectra can be summed, they are adjusted to a common energy-to-channel scale. This adjustment is done by shifting the spectra based on a preflight laboratory calibration of line location versus temperatures of the various electronic components in the signal chain. A second-order correction is made for long-term drift due to aging of components by summing together all of the adjusted spectra over a period of about a week and determining the difference in position of the lines from the standard locations. See *Boynton et al.* [2004] for a discussion of the nature of the gamma-ray spectra and an example of the improvement in signal-to-noise ratio for different accumulation times.

[11] For this work, the regions of interest are either 5° by 5° or 2° by 2° bins in a cylindrical grid on the Martian surface. These regions get smaller in area as they get closer to the poles, but they each contain approximately the same number of spectra because the spacecraft passes over these near-polar regions more frequently. The concentration of the elements on the surface is related directly to the intensity of their emission lines. However, for the lines produced via neutron interactions, it is not possible to simply invert the measured intensities to determine the concentration because the neutron flux is a function of composition. Instead, a forward model is generated to predict the flux of gamma rays for an assumed surface composition, the observations are compared to the predictions, and the concentration is adjusted as described below.

[12] The intensities of the gamma rays are determined from the areas of the peaks in each spectrum that is made by summing the spectra accumulated over each grid bin. The net area is the sum of the counts above the continuum formed by gamma rays that are scattered either in the detector or in the material between the detector and their point of generation. See *Evans et al.* [2006] for a detailed discussion of the analysis of gamma-ray spectra.

[13] In the case of gamma rays generated by neutron interactions, a correction to the peak areas is made to normalize them to the relative cosmic ray flux. This flux varies with time due both to changes during the 11-year solar cycle and to short-term changes in solar activity. The source of cosmic rays is from outside the solar system, and the varying magnetic field of the sun modulates the cosmic ray intensity and rates for nuclear reactions in the inner solar system [*Reedy*, 1987]. Even though we do not precisely know the absolute flux of cosmic rays, we can determine variations in the cosmic ray flux at the spacecraft by counting all events that deposit greater than 10 MeV of energy in the GS detector. Those few gamma rays with energy greater than 10 MeV are assumed to be related to cosmic ray interactions. The enhanced cosmic rays that enter the solar system during periods of low solar activity have a spectrum that is softer (lower energy) than the typical spectrum, so they are not so efficient at generating neutrons on the surface. By observing the relationship between intensity of the 1779 keV Si inelastic line and changes in the counts greater than 10 MeV, it was noted that the gamma signal differed by 60% of the estimated cosmic ray flux variation. This correction is applied to all of these data.

[14] Another correction that is made concerns background gamma rays that come from the instrument or the spacecraft. The background signal is determined from

spectra taken over the winter poles when CO_2 frost is thick enough to attenuate all, or nearly all, of the signal from that region of the planet [*Kelly et al.*, 2006]. The observed signal over the winter poles is analyzed to calculate the background count rate of the lines of interest, and these data are used to correct the relevant peak areas before they are used for analysis. Table 1 shows the gamma rays used for the analysis and the extent of the background correction made over the region between $\pm45°$ latitude. The correction, expressed as counts/second, is nearly constant over all of Mars, but it will obviously be a different fraction of the total depending on how much signal is coming from Mars over different regions.

[15] It is not generally appreciated that the intensities of the gamma rays coming from a planetary surface are very low. The count rate is low enough that each photon is counted and individually sorted by energy to generate the spectrum. As an example of the low counting rate of the gamma-ray photons, the count rate for the Si line at 1779 keV, which is one of the most intense gamma-ray lines used in this work, is 0.035 per second. Roughly a third of our 19.75-s spectra will not have a single count in the Si line peak. In addition, the peak occurs on a continuum that is about a factor 5 greater in magnitude. Clearly one needs long accumulation times to achieve a reasonable signal-to-noise ratio.

2.2. Calculation of Model Gamma-Ray Flux

[16] The first part of the process is to predict what the flux of gamma rays should be at the surface of the planet. For the radioactive elements, K and Th, the model calculation is straightforward. The surface emission rate can be simply calculated from an assumed model abundance of the element, the known disintegration rate for the gamma ray of interest, and the attenuation of that gamma ray from depth using mass attenuation coefficients from M. J. Berger et al. (XCOM: Photon cross sections database, 1990, http://physics.nist.gov/PhysRefData/Xcom/Text/XCOM.html) (hereinafter referred to as Berger et al., database, 1990) for a typical Mars surface composition. The composition used was based on the results of this work, but the attenuation is only weakly dependent on composition over the range observed on the surface. We assume that all elements, including K and Th, are homogeneous in the top few tens of centimeters of the surface.

[17] For the other elements, whose gamma rays are generated by interactions with neutrons, the calculation of expected surface flux is much more complicated. The gamma-ray fluxes of these elements are calculated by a forward model that depends on the flux of incident cosmic rays, the composition of the regolith, and the thickness and composition of the atmosphere. The production of neutrons was modeled with the Monte Carlo N-Particle eXtended code, MCNPX [*McKinney et al.*, 2006], for an incoming flux of cosmic rays that interact with the atmosphere and the surface. For this work we used a surface composition similar to that found for soil by Mars Pathfinder [*Wänke et al.*, 2001] altered to include rare earth elements (REE) by assuming a chondritic ratio of REE/Th and the average 0.6 ppm Th content of the soil from this work. The composition was further altered to include 3% H_2O, a typical value found by the GRS in the lower latitudes.

The output of the MCNPX calculation is the flux of neutrons as a function of energy and depth. From this output, we use the appropriate cross sections evaluated from the literature [*Kim et al.*, 2007] to calculate a table of gamma-ray fluxes at the surface as a function of cosine of emission angle (steps of 0.05) and atmospheric thickness (steps of 2 g/cm^2). Note that in this case the atmospheric thickness is important only because of its effect on the generation and moderation of neutrons, not for its attenuation of gamma rays; the effect of atmospheric attenuation is taken into account later. The emission angle is important for calculating the attenuation of gamma rays produced beneath the surface. Details on these calculations are given by *Kim et al.* [2007].

[18] For a given spacecraft location, the surface flux from each location on Mars that would be visible to the detector and contributing to the signal is determined by interpolation from this table for the appropriate atmospheric thickness and emission angle needed in the forward calculation. The calculated gamma-ray flux at the surface is then adjusted on the basis of orbital geometry and attenuation through the atmosphere to generate the flux at the spacecraft. The atmospheric attenuation is calculated from atmospheric thicknesses based on the Mars General Circulation Model of *Haberle et al.* [1999] and from mass attenuation coefficients from Berger et al. (database, 1990) applied to the composition of the Mars atmosphere. The atmospheric thickness is taken for the appropriate sol (Martian day) and approximate local time when the spectrum was collected, and it is corrected for variations due to elevation using data from the Mars Orbiter Laser Altimeter [*Smith et al.*, 2003]. Finally the calculated gamma-ray flux at the spacecraft is converted to counts based on the prelaunch measurements of efficiency as a function of angle and energy.

[19] The process of making these calculations is complex. The detector views a large area on the surface of the planet; different viewing angles from the detector will have different efficiencies, and depending on the angle, will view the planet through a different atmospheric thickness. The forward model calculates the expected counts in the detector for each of our 19.75-s-long spectra over every location on the planet on a grid of 0.5° by 0.5° cells. The location of the spacecraft over the surface of Mars at the midpoint of each spectrum is calculated, and the vectors from each cell on the surface to the spacecraft are determined.

[20] Though the GRS sees Mars from limb to limb (about 52 degrees of arc), for computational speed the calculations are limited to just the cells within a circle having a radius of 17 degrees of arc on the surface ($\sim$1000 km). Because of the large atmospheric attenuation of gamma rays at shallow slant angles, less than 1% of the signal comes from outside this circle. Even with this limit, it is necessary to separately do the calculation for 4,000 to 24,000 cells depending on the location of the spacecraft (e.g., more cells are within this circle closer to the poles).

2.3. Comparison Between Observed Flux and Modeled Flux to Determine Elemental Concentrations

[21] At the end of this process, each accumulated gamma-ray spectrum has associated with it a model calculation of the expected counts from each of about 40 gamma-ray lines of interest. In addition to the H, Si, Cl, K, Fe and Th lines,

there are lines for other elements, for example, O, Al, Ca, S, and U for which abundances will be evaluated in the future. When the gamma-ray spectra are summed together to generate a single spectrum for a particular $2° \times 2°$ or $5° \times 5°$ bin, the expected counts for each spectrum in the bin are similarly summed from the model-generated counts. The estimated abundance of an element in that bin is then determined by adjusting the model abundance by the ratio of the observed counts to the modeled counts for the line or lines indicative of that element. Where we have multiple gamma-ray lines for a given element (see Table 1), an average of all lines is calculated (weighted by the inverse square of the uncertainties). For the radioactive elements (K and Th), the process ends here. The estimated elemental abundance is the final elemental abundance. The results are plotted as a map after smoothing over different spatial scales depending on the element and its associated counting statistics as described in section 3.1.

[22] For the elements whose gamma rays are the result of nuclear interactions with cosmic ray-generated neutrons, further calculations are necessary. We use two different approaches depending on whether the gamma ray results from an interaction with fast neutrons, via inelastic scatter (Si), or with thermal neutrons, via capture (H, Cl, and Fe).

[23] For the inelastic scatter reaction on Si, we initially used the fast-neutron flux as measured by the neutron spectrometer (NS) component of the GRS to adjust the results under the assumption that the fast-neutron flux measured at the spacecraft could be directly related to the fast-neutron flux in the near surface where the gamma rays are generated [*Boynton et al.*, 2004]. By analyzing a large number of MCNPX runs with different surface compositions and atmospheric thicknesses, however, we found that the measured fast-neutron flux could not be related to the flux in the near surface in a simple manner without knowledge of the surface composition. For example, we found that at low H_2O contents compared to our nominal model, the fast neutron flux in orbit increased by 30% whereas the Si gamma-ray flux only increased by 8%. Clearly if we used the orbit-measured fast flux, we would overcorrect for variations in composition relative to our model soil by a substantial factor. Both the transport of the neutron measurements to the surface and the direct calculation of a gamma-ray correction factor described below require numerical modeling that is dependent upon composition. As discussed below, we decided to use the latter and not the NS measurements for correcting concentration data involving cosmic ray–generated neutrons.

[24] These model calculations, however, showed that there was a fairly simple relationship between the Si gamma-ray flux and the composition of the soil, mostly in variations in Fe and H content. (The Fe content is important because more neutrons per incident cosmic ray particle are made from Fe than from Ca and elements with atomic masses below about 40 Da [*Masarik and Reedy*, 1994]. H is important as it can readily slow neutrons [*Gasnault et al.*, 2001]). The results of these model calculations are shown in Figure 1. It can be seen that the correction factors for Fe and H are both independent of atmospheric thickness and both corrections are nearly linear over the range of compositions of interest. Not shown are other results demonstrating that the correction factors of Fe and H are independent of each

other, and that the correction of the observed range of Cl content is very small, on the order of 1% (relative, i.e., of the amount present). No correction is made for the effect of Cl on the Si flux.

[25] The absolute cosmic ray flux varies with time and is not well known, so it is necessary to normalize our results to some known elemental concentration. Silicon was chosen as our normalization element because it can be determined with good precision, and it is a major element which is expected to vary much less than other elements from place to place on the surface. We normalized our results to a value of 20.95% Si at the Mars Pathfinder landing site. See *Karunatillake et al.* [2007b] for a detailed discussion on how the lander values were determined from different soil and dust-free rock analyses made by the landers.

[26] For elements with gamma rays generated by thermal neutron capture, a somewhat different approach was used. As with the fast neutrons, we initially used the thermal neutron flux as measured by the NS to normalize our neutron-capture gamma-ray count rates. We found, however, that it was even more difficult to relate the observed orbital flux and surface fluxes for thermal neutrons than it was for the fast neutrons. On the basis of a large number of MCNPX model calculations, we found that the orbital flux of thermal neutrons was related to atmospheric thickness and to the concentration of H (a dominant neutron moderator as well as significant thermal neutron absorber) and Fe and Cl (both significant thermal neutron absorbers). These parameters interacted in a way that made it impossible to uniquely determine the concentration of H, Fe, and Cl from the observed orbital flux of thermal neutrons and the gamma rays associated with these elements. We tried using an iterative approach to solve for the concentrations of the elements, but the coupling between variations in different elements was sufficiently large that we could not get the results to converge.

[27] Fortunately, Si generates gamma rays from thermal neutron capture reactions in addition to the inelastic-scatter gamma ray discussed above. The approach adopted in this work for the elements determined from gamma rays produced via thermal neutron capture makes use of the fact that Si and the remaining reported elements, H, Cl, and Fe, have thermal neutron capture cross sections that vary nearly identically with energy. This characteristic is referred to as a 1/v cross section because the cross section increases inversely with the velocity of the neutron. Any variation in thermal neutron flux due to compositional differences in the soil will identically affect the gamma-ray flux of all such elements. The values of Si determined via the 1779 keV inelastic-scatter line at different places on the planet are considered the true Si values. We consider these Si values to be reliable because our extensive modeling studies showed its gamma flux depended only on H and Fe content, both of which we can determine with high accuracy. In addition, we found the standard deviation of all the Si values was only 0.8% Si, not much greater than our estimated precision based on counting statistics. We then take the ratio of apparent Si (determined via the neutron-capture gamma rays) to true Si (determined via the inelastic-scatter gamma ray) to be proportional to the relative thermal neutron flux just beneath the surface. This ratio, which is calculated after smoothing (see section 3 and Figures 2a, 2b and 2c) for
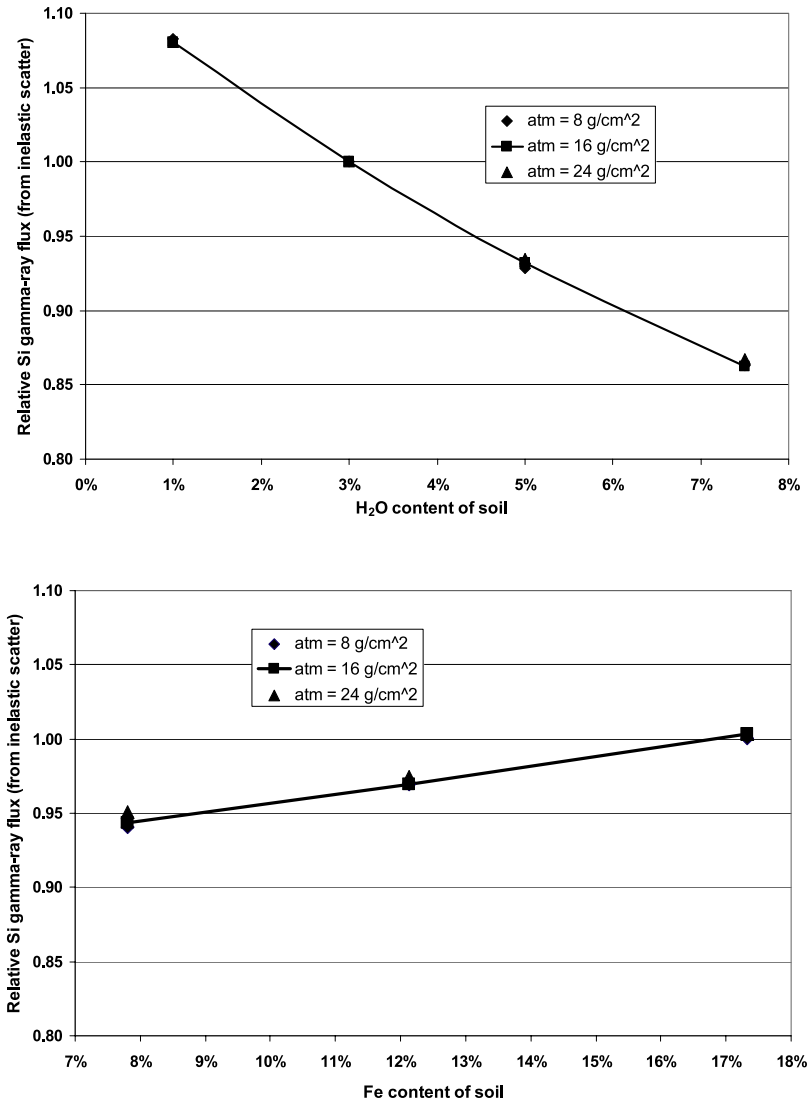
Figure 1. Relative signal from the Si inelastic gamma-ray line at different atmospheric thicknesses as a function of (top) H_2O and (bottom) Fe content in the soil. The Si signal has been corrected to a constant Si content. It can be seen that the gamma-ray flux is independent of atmospheric thickness and is nearly linearly dependent on Fe and H_2O content. These relationships are used to correct the observed Si inelastic gamma-ray flux to provide a measure of the true Si content on the surface.

every $0.5° \times 0.5°$ point on the surface, is then used to correct the H, Cl and Fe grid data for variations in thermal neutron flux.

[28] There is a small amount of circularity in this correction. The calculation of the amount of true Si depends on the concentration of Fe and H, but these elements are determined from the ratio of apparent Si to true Si. This circularity is very small, and it is resolved by iteration. Only one iteration is needed for the concentrations to converge to well under the statistical uncertainty.

3. Results

3.1. Smoothing of Binned Data and Making of Maps

[29] The spectra from the $2° \times 2°$ or $5° \times 5°$ bins from which the concentrations are calculated contain data of low statistical precision. It is therefore necessary to average data

from adjacent bins in order to improve the statistical precision in the data. There is a trade off between loss of spatial resolution by averaging too large an area versus lack of precision from averaging over too small an area. Figures 2a and 2b show a map of Si before and after smoothing where it can be seen that the map made from the unsmoothed $2° \times 2°$ bin data is very noisy.

[30] In order to determine if the elemental concentration of one particular part of the planet is statistically different from other locations, it is important to look at a measure of the statistical uncertainty of the data. Because the concentrations are ultimately determined by counting individual photons, we can calculate a statistical estimate of our precision based on Poisson statistics. For Si this uncertainty can also be seen in Figure 2b. The dependence of the uncertainty on elevation is obvious to those familiar with the topography of Mars. The lowest uncertainties occur in
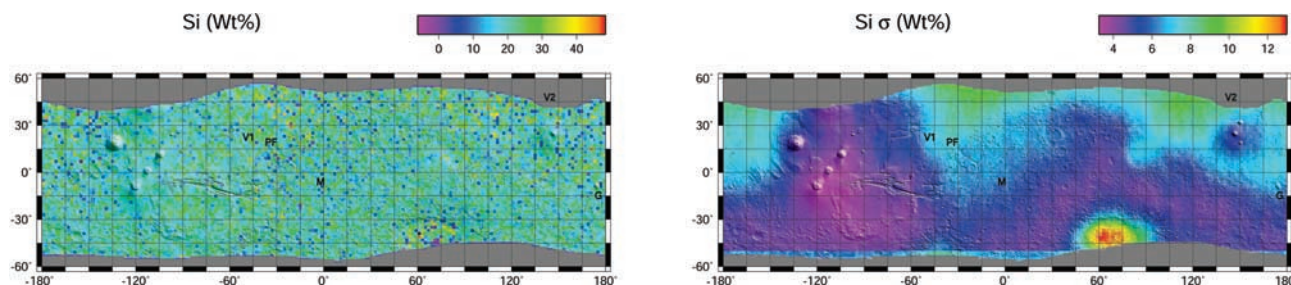
Figure 2a. Map of Si on a $2° \times 2°$ grid with no smoothing and before normalization and a map of its uncertainty (1 sigma). Note that the dynamic range of the unsmoothed data is very large as are their uncertainties. The landing sites are indicated (V1 and V2, Viking 1 and 2; PF, Mars Pathfinder; M and G, Meridiani and Gusev sites of the Mars Exploration Rovers). Data are not shown in regions of very high H content near the poles owing to the presence of subsurface ice that has a significant effect on the distribution of neutrons, which are the excitation source for all elements shown in this work except for K and Th.

areas of high elevation, for example, the southern highlands due to low attenuation of the signal by the atmosphere, and the highest uncertainties occur in areas of low elevation, for example, Hellas and the northern lowlands (see Figure 3 for locations of regions referred to in this and subsequent papers in this issue).

[31] The map of uncertainties shows the estimated 1-sigma uncertainty of the smoothed data; the uncertainties include the statistical uncertainties associated with estimating the area of the peaks in the spectrum. For Si they include the uncertainties associated with the corrections due to H and Fe, and for the capture lines, they include the uncertainties associated with the capture correction factors. In the case where one is interested in ratios of one capture line to another, for example, the Fe/Cl ratio, the uncertainties are lower. The uncertainties in the concentration of each element can be reduced by the uncertainties in the capture correction factors (Figure 2c) since these uncertainties are common to all capture elements.

[32] The maps shown in this work have been smoothed to varying degrees based on the dynamic range of the abundance of the element over the surface and the statistical precision in the binned data. Using a $0.5° \times 0.5°$ grid, the smoothing is performed through an arithmetic mean of all of the values within the smoothing radius (i.e., a boxcar filter). The extent of smoothing for each map is given in Table 1.

[33] The reader should be cautioned, however, that even in the smoothed maps, small areas of color difference, on the order of the size of the smoothing circle or smaller, may not reflect a meaningful compositional difference from the surrounding areas on the planet. It is important to check the corresponding map of uncertainty to test for the significance of a color difference. For example, in the smoothed map of Si (Figure 2b), a small red spot having a Si content of about 22% can be seen near 60° longitude and 45° latitude. The uncertainty map, however, shows that the uncertainty in this area is about 0.6% Si. Thus the red spot differs from the yellow surrounding area, corresponding to an Si abundance of about 21.7%, by less than 1 sigma (i.e., estimated standard error). On the other hand, the large yellow region to the west is larger than the smoothing circle, and as such, one would not expect so many nearby 1-sigma variations to be in the same direction. Thus this region can be considered to be significantly different from the surrounding green area even though the uncertainty for each point may be the same as it is for the former location. Another aspect of the maps is important for the reader to recognize. Because of the smoothing, the value plotted on the map is not necessarily the concentration of the element at that particular point. Rather, it is really the average concentration of a region, centered at that location, having a size of the smoothing circle. Smoothing tends to reduce the real dynamic range as
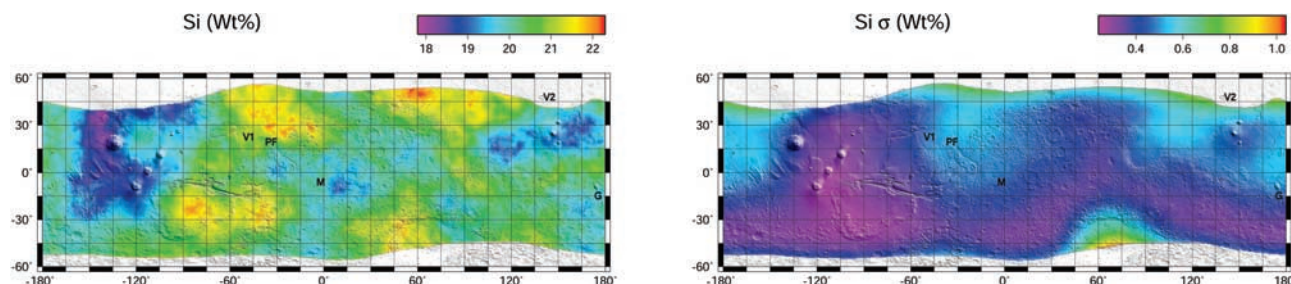

Figure 2b. Map of Si smoothed with a boxcar filter with a 15° radius. The Si concentrations are normalized to 20.95% Si at the PF landing site. The uncertainties range from about 0.3% Si to 0.6% Si over most of the planet. The difference in uncertainties is mainly due to differences in attenuation of the signal from the atmosphere; thus high-elevation regions have low uncertainties and low-elevation regions have high uncertainties.
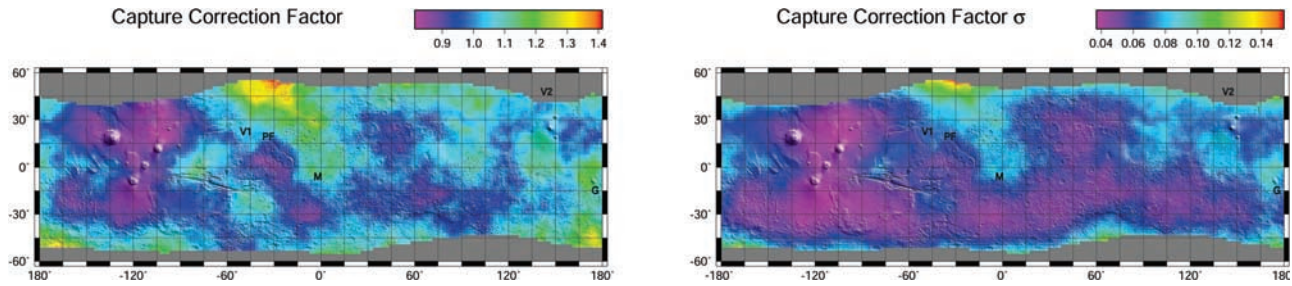
Figure 2c. Map of neutron-capture correction factors. This map is the ratio of Si (from Figure 2b) to apparent Si determined via thermal-neutron capture. The ratio accounts for the effect of different compositions on the thermal neutron flux just beneath the surface where the capture gamma rays are generated. For most of Mars the corrections are only on the order of 10%. As discussed in the text, the thermal neutrons measured at orbit are not a reliable measure of the flux of thermal neutrons beneath the surface.

well as to reduce the noise, and thus these effects need to be considered when interpreting the data from the maps.

3.2. Accuracy

[34] After normalization of the Si value at the Mars Pathfinder landing site, all other element values can be determined without further normalization to a ground truth. It is appropriate now to check to see how well the GRS-determined data agree with elemental compositions determined at other landing sites. This comparison is made in Table 2. See *Karunatillake et al.* [2007b] for a discussion of how the lander values were calculated from a mixture of soil and rocks at the different landing sites.

[35] Except for Fe, the agreement with the returned lander values is very good. This is remarkable considering that the lander values were determined over localities with spatial scale orders of magnitude smaller than the several hundred kilometers scale of the GRS data. It is important to keep in mind that reported concentrations for H, Si, Cl, and Fe are based upon only one normalization, i.e., that of Si to a value at Pathfinder. The values for K and Th are not normalized at all; they are simply calculated from known decay rates and the measured efficiency of the GRS sensor. In only three of the eleven independent cases, excluding Fe, does the difference between the GRS data and the lander data differ by more than two sigma. These results permit confidence that there are no large systematic errors in Si, Cl, and K. In addition, our determination of H, expressed as H_2O equivalent wt%, has been independently verified to agree with model calculations for the north polar region assuming the residual ice cap is 100% H_2O [*Boynton et al.*, 2007]. It is expected that Cl, H, and Fe would not show systematic errors relative to each other, because the cross section for thermal neutron capture on these elements is very well known, and that parameter should be the dominant expected source of systematic errors.

[36] If we average the results in Table 2, we see that the GRS FE values are about 20% higher than the lander values. On the other hand, if the global GRS Fe data are compared with the Fe content of the Martian meteorites, the mean and standard deviation of the GRS-determined Fe content is nearly identical to that of the meteorites [*Boynton et al.*, 2007]. Thus we feel the difference between the GRS data and the lander data for Fe is real and is attributed to an incomplete sampling of rocks and soil by the landers over the scale of the GRS footprint.

[37] To explore the question of Fe accuracy further, we investigated whether the systematic differences observed could be due to the fact that we could calibrate detector efficiency only up to 6129 keV, the highest energy source available for laboratory work. The efficiency at the two Fe lines used in this work (7129 and 7638 keV) had to be determined via extrapolation. To test if this extrapolation might be the source of the disparity, the Fe content in a spectrum summed over the entire planet between ±45° of latitude was determined for these two lines and for two additional lines (5920 and 9298 keV) that are normally too weak for routine analysis of the small grid areas used for mapping. We thus had four independent estimates of the average midlatitude Fe content from the four different lines. In this case, the results for the two additional lines agreed within one sigma with the results for the 7127 keV line, which is the 511 keV escape line generated in the detector from the loss of one of the positron annihilation photons. On the other hand, the 7638 keV line, the primary line that is the source of the 7127 keV line, was high by 10% when compared to the results of the other three lines. (Note that the 7638 keV line is actually a doublet of two closely spaced gamma rays at 7631 and 7645 keV.) The low-energy line at 5920 keV had an uncertainty of only 1.7% and, since it is within the energy region of laboratory calibration where an extrapolation of the detector efficiency was not needed, its result is considered more reliable. The very high energy line of Fe at 9298 keV has an uncertainty of 7.3% so it cannot be used independently to choose between the results of the 7638 and 7127 keV lines. However, since the midlatitude averages of the 5920, 7127 and 9298 keV lines agreed within one sigma while the average for the same area measured using the 7638 keV line was 10% high, we decided to use a single global normalization factor based on this ratio and apply it to all 7638 keV measurements. Thus our results for the Fe map are the weighted mean of the 7127 and normalized 7638 keV lines.

3.3. Maps

[38] The calculated adjustments to the Si inelastic flux are only valid in regions of low H content owing to the large effect of H on the moderation of neutron energies. Conse-
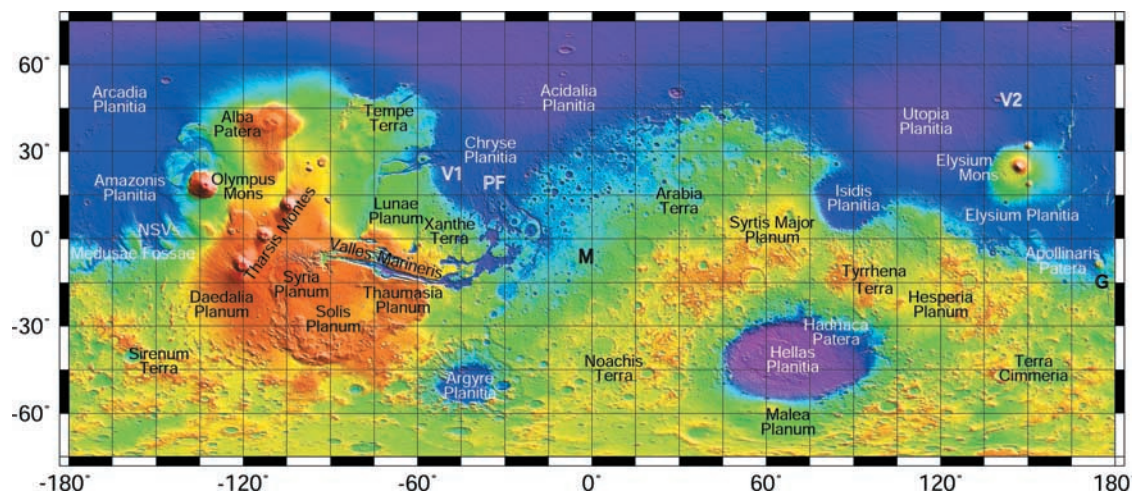
Figure 3. Locator map showing names and locations of features referenced in this work and in other manuscripts in this issue. Elevation data are from the Mars Orbiter Laser Altimeter [*Smith et al.*, 2003].

quently the high-latitude regions with high H_2O content cannot be analyzed quantitatively by this approach. We mask the data from all but the radioactive elements (the abundances of which are independent of the neutron flux) to exclude these regions. The mask is determined by filtering the raw H gamma-ray flux to emphasize the north-south gradient and eliminating the areas poleward of a flux contour equivalent to an H_2O content of 6%. This value of 6% was chosen to minimize the contribution to the signal from the polar regions of high H_2O content but to not exclude any of the lower latitude data near the polar region. The results are then smoothed with boxcar filters as noted in Table 1. In the case of the radioactive elements, the results are plotted up to ±75 degrees latitude, but it should be understood that the H_2O content in the high latitudes is sufficient to significantly dilute the content of K and Th. In addition, because the H_2O is substantially enriched in an ice layer beneath a relatively dry layer *Boynton et al.* [2002], the mapped abundance of K and Th in this region is a rough average of their abundances in the two layers.

[39] Except for H, the maps are all given in terms of the concentration, as a mass fraction, of the element, not of the oxide. In the case of Mars, it is clear that Fe can exist in both oxidation states (FeO and Fe_2O_3) and thus the oxidation state is not well known. For H, we have chosen to map it as H_2O because the presence of H_2O as a pure phase (ice and water) has clearly had a profound effect on the Martian surface, though it almost certainly does not exist as a pure phase in any of the low-latitude regions mapped in this work.

[40] The map products discussed below are available in a variety of electronic formats at http://grs.lpl.arizona.edu/data.

3.3.1. Silicon

[41] The map of Si (Figure 2b) shows only modest variation from place to place, as expected for this major rock-forming element. The Si content over most of the map ranges from 18.5% to 21.5% (39.6% to 46.0% as SiO_2). The standard deviation of these variations is only 0.8% Si (4% relative), which is comparable to the uncertainties in each point. This observation indicates that many of the small

differences observed in the map may not be statistically significant.

[42] The Elysium rise and surrounding regions and the younger parts of the Tharsis rise, including Tharsis Montes and Olympus Mons shield volcanoes, region around Tharsis Montes, however, shows significantly lower Si content, down to 17.8% along the central and northwest margins of Tharsis, perhaps being indicative of recent basaltic volcanism, though as discussed later with respect to potassium, other locations of young basaltic lava flows do not show a lower Si content [*Scott and Tanaka*, 1986; *Tanaka et al.*, 2005]. We see no region of a large enrichment in Si content that would indicate evolved rocks such as granite. Smaller regions, such as those observed by *Christensen et al.* [2005] which suggest such evolved rocks may have formed, are much smaller than the GRS footprint.

[43] The beginning of a high Si content near the northern edge of the mapped region near +50° lat, −35° lon can also be observed. Even though this region corresponds to the Surface Type 2 region based on data from the Thermal Emission Spectrometer instrument [*Bandfield et al.*, 2000], GRS data do not indicate a Si enhancement relative to Surface Type 1 [*Karunatillake et al.*, 2007a]. The relationship of these and other GRS data to the surface type 2 region are discussed in more detail in the work of *Karunatillake et al.* [2007a].

3.3.2. Iron

[44] The map of Fe (Figure 4a) shows an enrichment of Fe in the northern lowlands. The boundary of the enrichment closely follows the 0-km elevation contour, showing values ranging from 14% Fe to about 19% Fe in the lowlands (18% FeO to 24% FeO equivalent) versus 11% Fe to 14% Fe in the highlands (14% FeO to 18% FeO). As mentioned above in the discussion of accuracy, the Fe values are higher than the combined rock-plus-soil values from the landing sites, but agree well with the values of the Martian meteorites. (This difference cannot be due to an inaccurate correction for attenuation of the gamma rays caused by the atmosphere. We do not see a large variation in Si content between the highlands and lowlands even though

Table 2. Comparison of Values in Weight Percent From the Gamma Sensor (GS) in This Work With Values Determined From the Landers[a]

	Pathfinder	Viking-1	Spirit	Opportunity
Si				
Lander	21.0	22.6	18.4	20.2
σ	1.9	1.6	0.5	0.6
GS	21.0	20.9	19.6	19.8
σ	0.5	0.5	0.5	0.5
Difference	0.0	−1.7	1.2	−0.4
σ	2.0	1.7	0.7	0.8
Fe				
Lander	14.6	13.2	11.8	13.8
σ	0.9	1.3	0.3	0.7
GS	17.3	15.4	15.7	15.4
σ	1.3	1.2	1.2	1.3
Difference	2.7	2.2	3.9	1.6
σ	1.6	1.8	1.3	1.5
Cl				
Lander	0.49	0.71	0.72	0.466
σ	0.07	0.17	0.07	0.006
GS	0.37	0.37	0.68	0.59
σ	0.05	0.04	0.06	0.06
Difference	−0.12	−0.34	−0.04	0.12
σ	0.08	0.18	0.09	0.06
K				
Lander	0.63	0.22	0.284	0.336
σ	0.07	0.13	0.014	0.016
GS	0.42	0.32	0.328	0.316
σ	0.03	0.03	0.020	0.023
Difference	−0.21	0.10	0.044	−0.020
σ	0.08	0.13	0.024	0.028

[a]See *Karunatillake et al.* [2007b]; σ is the standard error.

the corrections for atmospheric attenuation of the Si gamma rays are larger than the ones for Fe.)

[45] We have GRS data with limited statistics on all of the other major elements (those with mass fractions exceeding 3%, i.e., Mg, Al, Si, Ca, Fe) except Mg, and none of them appear to show a relationship between highlands and lowlands. It is clear by mass balance that some elemental concentrations will need to decrease in concentration as Fe increases. The fact that we do not observe sufficient differences in the abundances of these other elements to account for the change in Fe concentration leads us to the tentative conclusion that Mg is varying inversely with Fe between the lowlands and the highlands. (Mg cannot be determined by the GRS because it, with Ti, is one of two elements used extensively in the mechanical construction of the instrument [*Boynton et al.*, 2004].)

[46] Because of the lack of correlation of other elements that might be expected to vary with Fe in normal igneous processes, we suggest that the cause of this Fe enrichment in the northern lowlands may be due to aqueous processes, including weathering. *Klingelhöfer et al.* [2004] and *Squyres et al.* [2004] have reported at the Opportunity landing site the existence of jarosite, a hydrated iron sulfate that forms only in highly acidic solutions. We speculate that acidic aqueous activity, including precipitation and infiltration in the southern highlands [*Craddock and Maxwell*, 1993; *Craddock and Howard*, 2002; *Scott et al.*, 1995; *Baker*, 2001] could leach Fe, which is relatively easily leached at low pH, from the surface and carry the weathering products deep into the regolith [*Fairén et al.*, 2004]. Subsequent hydrologic activity resulted in a transferal of weathered products from the cratered highlands to the lowlands, including via Tharsis- (and to a lesser extent Elysium-) induced flooding and deep dissection of the Martian crust to form outflow channels [e.g., *Baker et al.*, 1991; *Dohm et al.*, 2001a, 2001b; *Fairén et al.*, 2003], as well as spring-fed activity along the dichotomy boundary [*Tanaka et al.*, 2005].

3.3.3. Chlorine

[47] The map of Cl (Figure 4b) shows significant variation over the mid latitudes. Most notable is the significant enrichment west of the Tharsis Montes and northeast of Apollinaris Patera where the Cl mass fraction exceeds 0.8%. The greatest part of this enrichment is over Medusae Fossae Formation materials, interpreted to be ignimbrite deposits [*Malin*, 1979; *Scott and Tanaka*, 1982] among other interpretations [*Zimbelman et al.*, 1997]. Geologically young (Middle to Late Amazonian; see *Scott and Tanaka* [1986] for details on the time-stratigraphic age assignments of Mars), Medusae Fossae Formation materials reveal predominantly wind-etched surface morphologies suggesting exhumation, though the materials are dissected, in places, by valleys [*Scott et al.*, 1995]. This region of high Cl concentration may result from deposition of Cl (e.g., Cl-enriched materials which are subsequently eroded) and/or may be associated with the release of Cl through volcanic exhalations.

[48] Areas of moderately high Cl include a band that closely follows the dichotomy boundary west of the Tharsis
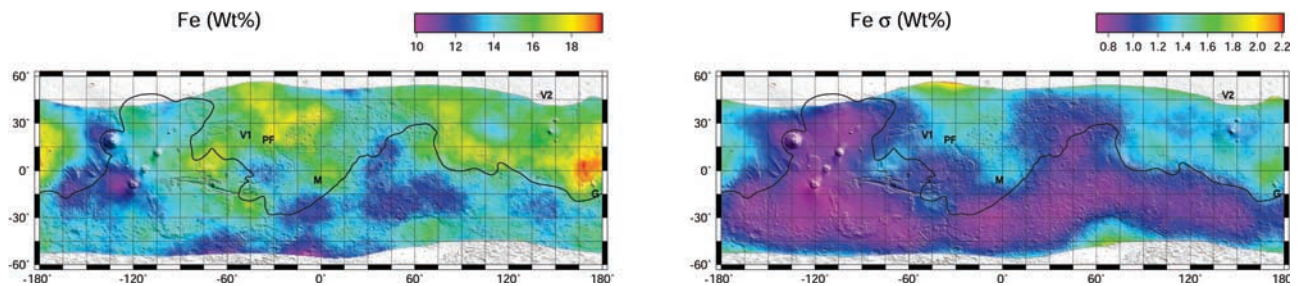

Figure 4a. Map of Fe concentrations and their uncertainties in the low and mid latitudes of Mars. A substantial enrichment of Fe is observed in the northern lowlands, north of the 0-km elevation contour shown. This enrichment may be due to acidic aqueous activity, which could leach Fe from the surface so that it could ultimately be transported to the lowlands via hydrologic activity.
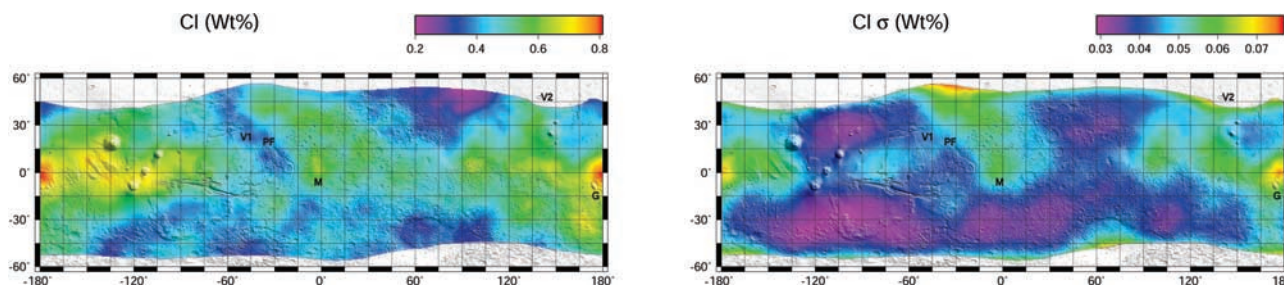
Figure 4b. Map of Cl concentrations and their uncertainties in the low and mid latitudes of Mars. A substantial enrichment of Cl is observed in the Medusae Fossae Formation. This enrichment may be associated with ignimbrite deposits in this area, or may be due to Cl-rich volcanic gases. In addition, moderately high amounts of Cl are found in Arabia Terra and in a band that follows the dichotomy boundary west of the Tharsis Montes. These latter regions show increased H_2O content as well (see Figure 4c).

Montes shield volcanoes (including the highly Cl-enriched region located northeast of Apollinaris Patera) and a region of moderately high Cl over Arabia Terra where the Cl contents are in the range of 0.5% Cl to 0.6% Cl. These more modest enrichments are similar to the distribution seen in the abundances of hydrogen discussed below. The global distribution of Cl correlates positively with hydrogen and negatively with Si and thermal inertia [*Keller et al.*, 2007]. The region of lowest Cl concentration (down to 0.22% Cl) is found to the north of Syrtis Major extending into Utopia Planitia. Possible mechanisms influencing the distribution of Cl measured at the Martian near-surface are discussed in more detail by *Keller et al.* [2007].

3.3.4. Hydrogen

[49] The map of H (Figure 4c), expressed as H_2O, shows more variation than any other element in the lower latitudes. The H_2O content ranges over a factor of 5, from about $1.5 \pm 0.3\%$ to $7.5 \pm 0.6\%$. The map shows an enrichment of H_2O in Arabia Terra and in the Medusae Fossae formation, especially near Apollinaris Patera. This seemingly isolated prominent shield volcano has been reported to be a location of significant magma-water interactions [*Scott et al.*, 1993; *Robinson et al.*, 1993], so the high H_2O content is consistent with this suggested geological history. Relationships between the map of H_2O and Cl are discussed below.

[50] A previously published map of H_2O determined via epithermal neutrons detected by the Neutron Spectrometer component of the GRS [*Feldman et al.*, 2004] shows a similar distribution of H_2O, but the absolute amount reported in that work is somewhat higher with a range from $2.0 \pm 0.3\%$ to $9.8 \pm 1.5\%$ H_2O [*Feldman et al.*, 2004]. Both results are based on similar assumptions of the model composition, i.e., a uniform distribution of elements within the footprint, both laterally and vertically, and a major-element composition similar to that found by Mars Pathfinder. In both cases the expected flux (of epithermal neutrons or H gamma rays) were calculated for different contents of H_2O and atmospheric thicknesses. These values agree with the values determined in this work to within 2 sigma, but there could still be some systematic difference between the two data sets.

[51] The differences in the results may be due to incorrect assumptions about the distribution of the elements in the footprint. If the H_2O is not uniformly distributed with depth but is layered with greater amounts of H_2O beneath the surface, as suggested by *Feldman et al.* [2005], the effect is actually to reduce the value derived from the GS data, so layering of the surface with enhanced H_2O beneath the surface cannot explain the discrepancy. Another possible difference between the model assumptions and reality could be a heterogeneous spatial distribution of H_2O on the surface; that is, parts of the surface within the GRS footprint could have very different H_2O contents. (The footprint of the NS is actually somewhat larger than that of the GS.) Because of the curvature in the power law relationship between H_2O content and epithermal flux [*Feldman et al.*, 2005], if there is lateral variation in the distribution of H_2O, the epithermal neutrons will consistently underestimate the true average amount of H_2O. The relationship between H gamma flux and H_2O content, on the other hand, is nearly linear, so the GS data would return a value very close to the true average. Thus heterogeneous lateral distribution within the footprint cannot explain the discrepancy either.

[52] It could be that the discrepancy is either not really significant or it is a systematic calibration error in one or both sets of data. As discussed above, however, the agreement with the lander data and the agreement with the H_2O content inferred for the north polar residual cap give us confidence that any systematic error with the GS data is small.

3.3.5. Comparison of H_2O and Cl Maps

[53] Noteworthy is the similarity among the maps of H_2O and Cl, where both show enrichments in Arabia Terra and near Apollinaris Patera. A band of moderate H_2O and Cl content runs along the dichotomy boundary west of Tharsis Montes, dividing regions of lower content both to the north and south. The most obvious big difference between the two maps is that Medusae Fossae shows a significant enrichment of Cl as noted earlier, but it does not show a comparably large increase in H_2O. This observation clearly points to a different source of Cl for the Medusae Fossae Formation than that distributed over much of the rest of Mars where H and Cl are highly correlated. The strong relationship between H and Cl in regions other than Medusae Fossae, suggest that both elements moved together, almost certainly because of a weathering-related process.
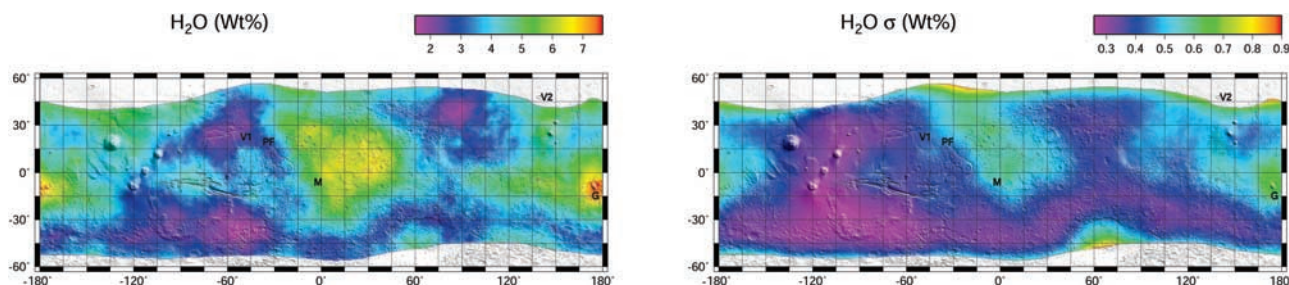
Figure 4c. Map of H_2O concentrations and their uncertainties in the low and mid latitudes of Mars. The H_2O content ranges over a factor of 5. It has a high content over Arabia Terra, in the Medusae Fossae Formation, and near Apollinaris Patera. These enrichments occur in the same areas as the enrichment in Cl. There is a major difference, however, with the Cl data showing a much greater enrichment in Medusae Fossae than the other regions. This extra enrichment is thought to be due to volcanism associated with the Tharsis Montes. The close relationship between Cl and H_2O in other areas is probably due to a weathering-related process.

3.3.6. Potassium and Thorium

[54] K and Th are highly correlated on Mars [*Karunatillake et al.*, 2007a; *Taylor et al.*, 2006a, 2006b], but are not uniformly distributed (Figures 5a and 5b). The northern plains from about −60°E to 180°E are rich in both, though the higher-than-average Th region extends much further south into the highlands. Both are generally medium to low over Tharsis. There is distinctly higher K and Th in the highlands in the region 15°E to 45°E, and extending from −150°E to +165°E. The region west of Hellas contains average K, but has relatively high Th.

[55] There are several areas in which the K and Th contents are significantly lower than the mean value, having concentrations less than 0.25% K. Examples include Hadriaca Patera (east of Hellas Planitia), the area east-southeast of Elysium Mons, Syria, and Solis Planae. These areas have been geologically mapped and interpreted as volcanic materials (including basaltic lava flows) (e.g., *Crown et al.* [1992], *Tanaka et al.* [2005], and *Dohm et al.* [2001c], respectively). The association of lower K with later (Hesperian and Amazonian) volcanism is suggestive of early formation of a crust enriched in incompatible elements, with the later magmas being derived from a depleted mantle, as previously suggested by *Norman* [1999, 2002] and *McLennan* [2003] from Martian meteorite data. This is discussed in detail by *Taylor et al.* [2006a] in the context of our GRS data.

[56] There is a very significant enhancement of K and Th in a portion of the northern lowlands. This enhancement corresponds closely to the surface type-2 region of *Bandfield et al.* [2000]. This region has been suggested to be andesitic in composition [*Bandfield et al.*, 2000] or to be a region of weathered basalt [*Wyatt and McSween*, 2002], or potentially consist of a different primary mineralogy with Si enhancement due to thin alteration coatings [*Rogers and Christensen*, 2007]. The relationship between GRS data and surface types 1 and 2 is discussed in more detail by *Karunatillake et al.* [2007a]. Part of this high-K region appears to be masked by a pronounced unit to the northwest of Elysium Mons. The low K content in this area matches closely the region mapped as a series of lahars by *Christiansen* [1989], showing the effect of the lower K from the more recent Elysium flows.

[57] The K/Th ratio varies by somewhat over a factor of two, but about 95% of the surface area is between 4000 and 7000 [*Taylor et al.*, 2006a, 2006b]. It is distinctly low west of Olympus Mons in Amazonis Planitia, in the region where Kasei Valles meets Chryse Planitia, in western Arabia Terra, and in Syrtis Major Planum. K/Th is high in Valles Marineris and surrounding region, Terra Cimmeria, and in the Hellas basin. These modest variations (most are within 1-sigma of the mean) may reflect a combination of bulk Martian K and Th concentrations, variations in the composition of the mantle source regions that produced lavas, and aqueous-related processes, including alteration, erosion, and deposition [*Taylor et al.*, 2006a]. However, the most striking feature of the distribution of K/Th values is their relative uniformity, making it a useful parameter to use when assessing models for the bulk composition of Mars [*Taylor et al.*, 2006b].

3.4. Overview

[58] Perhaps one of the more remarkable findings of this work is that there is no evidence for a globally distributed dust of uniform composition with a thickness on the order of tens of centimeters. A globally homogeneous dust or soil composition was expected to be present on the Martian surface, on the basis of similarities in the soils at the MER and Pathfinder and Viking landing sites [*Yen et al.*, 2005]. There is a current aeolian dust component that occurs as thin (easily churned up by rover wheels) bright dust observed at the MER landing sites [*Yen et al.*, 2005] and which also occurs over large areas of Mars as seen in remote sensing observations [*Putzig et al.*, 2005]. However, the GRS results suggest that this presumably homogeneous bright material is variable in composition, or is less than 10s of cm thickness over most areas. For example, *Newsom et al.* [2007] studied large areas thickly mantled with many meters of dust, including Arabia and Tharsis [*Arvidson et al.*, 2002]. These areas have similar reflectance spectra [*Putzig et al.*, 2005], but are significantly different in chemical composition. The composition of the surficial materials in the mantled regions, therefore, reflect a combination of derivation from local source rocks with different compositions or the effects of chemical alteration and chemical transport, either of the dust itself, or of the local source
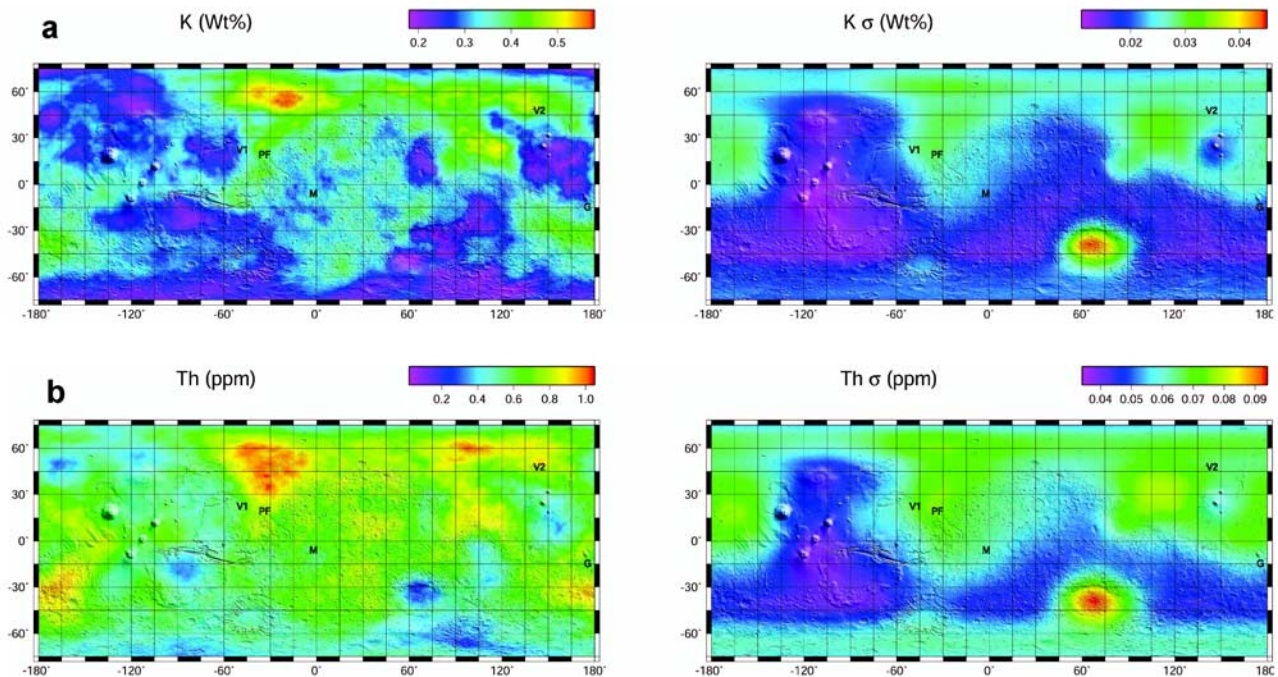
Figure 5. Maps of (a) K and (b) Th concentrations and their uncertainties in the low and mid latitudes of Mars. These elements are highly correlated on Mars, but they are not uniformly distributed. The K and Th contents are low in areas of young volcanic flows, Hadriaca Patera, the area east-southeast of Elysium Mons, Syria, and Solis Planae, suggestive of early crust formation enriched in incompatible elements, with the later magmas being derived from a depleted mantle. There is an enhancement of K and Th in a portion of the northern lowlands that corresponds closely to the surface type-2 region of *Bandfield et al.* [2000]. Part of this high-K region is masked by a unit to the northwest of Elysium Mons in the area that matches closely the region mapped as a series of lahars by *Christiansen* [1989].

rocks. See *Newsom et al.* [2007] for a more detailed discussion of the relationship between GRS data and dust on Mars, especially for the heavily mantled regions.

4. Summary

[59] This work presents an introduction to the rich data set available from the GS part of the GRS instrument suite. The concentrations of the elements presented are accurately determined from orbit and can be used to constrain (and formulate new) hypotheses concerning the processes that affected the planet since its formation [e.g., *Taylor et al.*, 2006b]. As another example, we have begun to delineate chemically striking regions on Mars [*Taylor et al.*, 2007; *Keller et al.*, 2007; *Gasnault*, 2006] (also S. Karunatillake et al., The Mars Odyssey Gamma Ray Spectrometer reveals chemically striking regions on Mars, available at http://www.lpi.usra.edu/meetings/7thmars2007/pdf/3190.pdf).

[60] Future work should permit the construction of maps for Ca and Al, and perhaps for S and U, though the latter two have very weak signals and may not be mappable with a sufficient signal-to-noise ratio to be useful. For example, for the most intense gamma ray from S we only count one photon every three minutes. We can, however, generate spectra over large regions, for example, Arabia Terra or the southern highlands, and determine an average S content for those regions. We are hopeful that as the community, including the GRS team, gets accustomed to using these

data, more insight into the processes that shaped the present-day Mars will be generated.

References

Arvidson, R. E., P. R. Christensen, J. Garvin, and M. Mellon (2002), On the distribution and implications of mantled and exhumed terrains on Mars, paper presented at *Solar System Remote Sensing Symposium*, Lunar and Planet. Inst., Houston, Tex.

Baird, A. K., A. J. Castro, B. C. Clark, P. Toulmin III, H. Rose Jr., K. Keil, and J. L. Gooding (1977), The Viking X Ray Fluorescence Experiment: Sampling strategies and laboratory simulations, *J. Geophys. Res.*, *82*, 4596–4624.

Baker, V. R. (2001), Water and the Martian landscape, *Nature*, *412*, 228–236.

Baker, V. R., R. G. Strom, V. C. Gulick, J. S. Kargel, G. Komatsu, and V. S. Kale (1991), Ancient oceans, ice sheets and the hydrological cycle on Mars, *Nature*, *352*, 589–594.

Bandfield, J. L. (2002), Global mineral distributions on Mars, *J. Geophys. Res.*, *107*(E6), 5042, doi:10.1029/2001JE001510.

Bandfield, J. L., V. E. Hamilton, and P. R. Christensen (2000), A global view of Martian surface compositions from MGS-TES, *Science*, *287*, 1626–1630.

Bell, J. F., et al. (2000), Mineralogical and compositional properties of Martian soil and dust: Results from Mars Pathfinder, *J. Geophys. Res.*, *105*, 1721–1755.

Bibring, J.-P., et al. (2005), Mars surface diversity as revealed by the OMEGA/Mars Express, *Science*, *307*, 1576–1581.

Bielefeld, M. J., R. C. Reedy, A. E. Metzger, J. I. Trombka, and J. R. Arnold (1976), Surface chemistry of selected lunar regions, *Proc Lunar Sci. Conf.*, *7th*, 2661–2676.

Boynton, W. V., et al. (1992), Science applications of the Mars Observer Gamma Ray Spectrometer, *J. Geophys. Res.*, 97, 7681–7698.

Boynton, W. V., et al. (2002), Distribution of hydrogen in the near surface of Mars: Evidence for subsurface ice deposits, *Science*, 297, 81–85.

Boynton, W. V., et al. (2004), The Mars Odyssey Gamma-Ray Spectrometer Instrument Suite, *Space Sci. Rev.*, 110, 37–83.

Boynton, W. V., G. J. Taylor, S. Karunatillake, R. C. Reedy, and J. M. Keller (2007), Elemental abundances determined via the Mars Odyssey GRS, in *The Martian Surface: Composition, Mineralogy, and Physical Properties*, edited by J. F. Bell III, chap. 5, Cambridge Univ. Press, New York, in press.

Christensen, P. R., et al. (2001), The Mars Global Surveyor Thermal Emission Spectrometer experiment: Investigation description and surface science results, *J. Geophys. Res.*, 106, 23,823–23,871.

Christensen, P. R., et al. (2005), The igneous diversity of Mars: Evidence for magmatic evolution analogous to Earth, *Lunar Planet. Sci.*, 36, abstract 1273.

Christiansen, E. H. (1989), Lahars in the Elysium region of Mars, *Geology*, 17, 203–206.

Clark, B. C., III, A. K. Baird, H. J. Rose Jr., P. Toulmin III, R. P. Christian, W. C. Kelliher, A. J. Castro, C. D. Rowe, K. Keil, and G. R. Huss (1977), The Viking X ray fluorescence experiment: Analytical methods and early results, *J. Geophys. Res.*, 82, 4577–4594.

Clark, B. C., et al. (2005), Chemistry and mineralogy of outcrops at Meridiani Planum, *Earth Planet. Sci. Lett.*, 240, 73–94.

Craddock, R. A., and A. D. Howard (2002), The case for rainfall on a warm, wet early Mars, *J. Geophys. Res.*, 107(E11), 5111, doi:10.1029/2001JE001505.

Craddock, R. A., and T. A. Maxwell (1993), Geomorphic evolution of the Martian highlands through ancient fluvial processes, *J. Geophys. Res.*, 98, 3453–3468.

Crown, D. A., K. H. Price, and R. Greeley (1992), Geologic evolution of the east rim of the Hellas basin, Mars, *Icarus*, 100, 1–25.

Davis, P. A. (1980), Iron and titanium distribution on the Moon from orbital gamma-ray spectrometry with implications for crustal evolutionary models, *J. Geophys. Res.*, 85, 3209–3224.

Dohm, J. M., J. C. Ferris, V. R. Baker, R. C. Anderson, T. M. Hare, R. G. Strom, N. G. Barlow, K. L. Tanaka, J. E. Klemaszewski, and D. H. Scott (2001a), Ancient drainage basin of the Tharsis region, Mars: Potential source for outflow channel systems and putative oceans or paleolakes, *J. Geophys. Res.*, 106, 32,943–32,958.

Dohm, J. M., et al. (2001b), Latent activity for western Tharsis, Mars: Significant flood record exposed, *J. Geophys. Res.*, 106, 12,301–12,314.

Dohm, J. M., K. L. Tanaka, and T. M. Hare (2001c), Geologic map of the Thaumasia region of Mars, *Map, I-2650*, U.S. Geol. Surv., Boulder, Colo.

d'Uston, C., et al. (1989), Observation of the γ-ray Emission From the Martian surface by the APEX experiment, *Nature*, 341, 598–600.

Evans, L. G., and S. W. Squyres (1987), Investigation of Martian H₂O and CO₂ via orbital gamma ray spectroscopy, *J. Geophys. Res.*, 92, 9153–9167.

Evans, L. G., R. C. Reedy, and J. I. Trombka (1993), Introduction to planetary remote sensing gamma ray spectroscopy, in *Remote Geochemical Analyses: Elemental and Mineralogical Composition*, edited by C. M. Pieters and P. A. J. Englert, pp. 167–198, Cambridge Univ. Press, New York.

Evans, L. G., R. C. Reedy, R. D. Starr, K. E. Kerry, and W. V. Boynton (2006), Analysis of gamma-ray spectra measured by Mars Odyssey, *J. Geophys. Res.*, 111, E03S04, doi:10.1029/2005JE002657.

Fairén, A. G., J. M. Dohm, V. R. Baker, M. A. de Pablo, J. Ruiz, J. C. Ferris, and R. C. Anderson (2003), Episodic flood inundations of the northern plains of Mars, *Icarus*, 165, 53–67.

Fairén, A. G., D. Fernández-Remolar, J. M. Dohm, V. R. Baker, and R. Amils (2004), Inhibition of carbonate synthesis in acidic oceans on early Mars, *Nature*, 431, 423–426.

Feldman, W. C., et al. (2002), Global distribution of neutrons from Mars: Results from Mars Odyssey, *Science*, 297, 75–78.

Feldman, W. C., et al. (2004), Global distribution of near-surface hydrogen on Mars, *J. Geophys. Res.*, 109(E9), E09006, doi:10.1029/2003JE002160.

Feldman, W. C., et al. (2005), Topographic control of hydrogen deposits at low latitudes to midlatitudes of Mars, *J. Geophys. Res.*, 110, E11009, doi:10.1029/2005JE002452.

Fialips, C. I., J. W. Carey, D. T. Vaniman, D. L. Bish, W. C. Feldman, and M. T. Mellon (2005), Hydration state of zeolites, clays, and hydrated salts under present-day Martian surface conditions: Can hydrous minerals account for Mars Odyssey observations of near-equatorial water-equivalent hydrogen?, *Icarus*, 178, 74–83.

Gasnault, O. (2006), Unsupervised definition of chemically distinct provinces at Mars, *Lunar Planet Sci.*, 37, abstract 2328.

Gasnault, O., W. C. Feldman, S. Maurice, I. Genetay, C. D'Uston, T. H. Prettyman, and K. R. Moore (2001), Composition from fast neutrons: Application to the Moon, *Geophys. Res. Lett.*, 28(19), 3797–3800.

Gellert, R., et al. (2004), Chemistry of rocks and soils in Gusev Crater from the Alpha Particle X-ray Spectrometer, *Science*, 305, 829–832.

Gellert, R., et al. (2006), Alpha Particle X-Ray Spectrometer (APXS): Results from Gusev crater and calibration report, *J. Geophys. Res.*, 111, E02S05, doi:10.1029/2005JE002555.

Gendrin, A., N. Mangold, J. P. Bibring, Y. Langevin, B. Gondet, F. Poulet, G. Bonello, C. Quantin, J. Mustard, R. Arvidson, and S. LeMouelic (2005), Sulfates in Martian layered terrains: The OMEGA/Mars Express view, *Science*, 307, 1587–1591.

Haberle, R. M., M. M. Joshi, J. R. Murphy, J. R. Barnes, J. T. Schofield, G. Wilson, M. Lopez-Valverde, J. L. Hollingsworth, A. F. C. Bridger, and J. Schaeffer (1999), General circulation model simulations of the Mars Pathfinder atmospheric structure investigation/meteorology data, *J. Geophys. Res.*, 104, 8957–8974.

Karunatillake, S., et al. (2007a), Composition of northern low albedo regions of Mars: Insights from the Mars Odyssey Gamma Ray Spectrometer, *J. Geophys. Res.*, 112, E03S05, doi:10.1029/2006JE002675.

Karunatillake, S. K., J. M. Keller, S. W. Squyres, W. Boynton, J. Brückner, D. M. Janes, O. Gasnault, and H. E. Newsom (2007b), Chemical compositions at Mars landing sites subject to Mars Odyssey Gamma Ray Spectrometer constraints, *J. Geophys. Res.*, 112, E08S90, doi:10.1029/2006JE002859.

Keller, J. M., et al. (2007), Equatorial and mid-latitude distribution of chlorine measured by Mars Odyssey GRS, *J. Geophys. Res.*, 112, E03S08, doi:10.1029/2006JE002679.

Kelly, N. J., W. V. Boynton, K. Kerry, D. Hamara, D. Janes, R. C. Reedy, K. J. Kim, and R. M. Haberle (2006), Seasonal polar carbon dioxide frost on Mars: CO₂ mass and columnar thickness distribution, *J. Geophys. Res.*, 111, E03S07, doi:10.1029/2006JE002678. [Printed 112(E3), 2007].

Kim, K. J., D. M. Drake, R. C. Reedy, R. M. S. Williams, and W. V. Boynton (2007), Theoretical fluxes of gamma rays from the Martian surface, *J. Geophys. Res.*, 112, E03S09, doi:10.1029/2005JE002655.

Klingelhöfer, G., et al. (2004), Jarosite and hematite at Meridiani Planum from Opportunity's Mössbauer Spectrometer, *Science*, 306, 1740–1745.

Lawrence, D. J., W. C. Feldman, B. L. Barraclough, A. B. Binder, R. C. Elphic, S. Maurice, and D. R. Thomsen (1998), Global elemental maps of the Moon: The Lunar Prospector Gamma-Ray Spectrometer, *Science*, 281, 1484–1489.

Litvak, M. L., I. G. Mitrofanov, A. S. Kozyrev, A. B. Sanin, V. I. Tretyakov, W. V. Boynton, N. J. Kelly, D. Hamara, C. Shinohara, and R. S. Saunders (2006), Comparison between polar regions of Mars from HEND/Odyssey data, *Icarus*, 180, 23–27.

Malin, M. C. (1979), Mars: Evidence of indurated deposits of fine materials, *NASA Conf. Publ.*, 2072, 54 pp.

Masarik, J., and R. C. Reedy (1994), Effects of bulk composition on nuclide production processes in meteorites, *Geochim. Cosmochim. Acta*, 58, 5307–5317.

Masarik, J., and R. C. Reedy (1996), Gamma ray production and transport in Mars, *J. Geophys. Res.*, 101, 18,891–18,912.

McKinney, G. W., D. J. Lawrence, T. H. Prettyman, R. C. Elphic, W. C. Feldman, and J. J. Hagerty (2006), MCNPX benchmark for cosmic ray interactions with the Moon, *J. Geophys. Res.*, 111, E06004, doi:10.1029/2005JE002551.

McLennan, S. M. (2003), Large-ion lithophile element fractionation during the early differentiation of Mars and the composition of the Martian primitive mantle, *Meteorit. Planet. Sci.*, 38, 895–904.

McSween, H. Y., et al. (2004), Basaltic rocks analyzed by the Spirit Rover in Gusev Crater, *Science*, 305, 842–845.

Merényi, E., R. B. Singer, and J. S. Miller (1996a), Mapping of spectral variations on the surface of Mars from high spectral resolution telescopic images, *Icarus*, 124, 280–295.

Merényi, E., K. S. Edgett, and R. B. Singer (1996b), Deucalionis Regio, Mars: Evidence for a new type of immobile, weathered soil unit, *Icarus*, 124, 296–307.

Mitrofanov, I., et al. (2002), Maps of subsurface hydrogen from the high energy neutron detector, Mars Odyssey, *Science*, 297, 78–81.

Mitrofanov, I. G., et al. (2004), Soil water content on Mars as estimated from neutron measurements by the HEND instrument onboard the 2001 Mars Odyssey spacecraft, *Sol. Syst. Res.*, 38(4), 253–265.

Morris, R. V., et al. (2000), Mineralogy, composition, and alteration of Mars Pathfinder rocks and soils: Evidence from multispectral, elemental, and magnetic data on terrestrial analogue, SNC meteorite, and Pathfinder samples, *J. Geophys. Res.*, 105, 1757–1818.

Newsom, H. E., et al. (2007), Geochemistry of Martian soil and bedrock in mantled and less mantled terrains with gamma ray data from Mars Odyssey, *J. Geophys. Res.*, 112, E03S12, doi:10.1029/2006JE002680.

Norman, M. D. (1999), The composition and thickness of the crust of Mars estimated from rare earth elements and neodymium-isotopics of Martian meteorites, *Geochim. Cosmochim. Acta, 34,* 439–449.

Norman, M. D. (2002), Thickness and composition of the Martian crust revisited: Implications of an ultradepleted mantle with a Nd isotopic composition like that of QUE94,201, *Lunar Planet. Sci., XXXIII,* abstract 1175.

Putzig, N. E., M. T. Mellon, K. A. Kretke, and R. E. Arvidson (2005), Global thermal inertia and surface properties of Mars from the MGS mapping mission, *Icarus, 173,* 325–341.

Reedy, R. C. (1987), Nuclide production by primary cosmic-ray protons. in: *Proc. Lunar Planet. Sci. Conf. 17th,* Part 2, *J. Geophys. Res., 92,* E697–E702, suppl.

Rieder, R., et al. (2004), Chemistry of rocks and soil at Meridiani Planum from the Alpha Particle X-ray Spectrometer, *Science, 306,* 1746–1749.

Robinson, M. S., P. J. Mouginis-Mark, J. R. Zimbelman, S. S. C. Wu, K. K. Ablin, and A. E. Howington-Kraus (1993), Chronology, eruption duration, and atmospheric contribution of the Martian volcano Apollinaris Patera, *Icarus, 104,* 301–323.

Rogers, D., and P. Christensen (2007), Surface mineralogy of Martian low-albedo regions from MGS-TES data: Implications for upper crustal evolution and surface alteration, *J. Geophys. Res., 112,* E01003, doi:10.1029/2006JE002727.

Saunders, R. S., et al. (2004), 2001 Mars Odyssey mission summary, *Space Sci. Rev., 110,* 1–36.

Scott, D. H., and K. L. Tanaka (1982), Ignimbrites of Amazonis Planitia region of Mars, *J. Geophys. Res., 87,* 1179–1190.

Scott, D. H., and K. L. Tanaka (1986), Geologic map of the western equatorial region of Mars, *Map I-1802-A,* 1:15,000,000, U.S. Geol. Surv., Boulder, Colo.

Scott, D. H., J. M. Dohm, and D. J. Applebee (1993), Geologic map of science study area 8, Apollinaris Patera region of Mars, *Map I-2351,* 1:500,000, U. S. Geol. Surv., Boulder, Colo.

Scott, D. H., J. M. Dohm, and J. W. Rice Jr. (1995), Map of Mars showing channels and possible paleolake basins, *USGS Misc. Inv. Ser. Map I-2461 (1:30,000,000).*

Singer, R. B., R. N. Clark, T. B. McCord, J. B. Adams, and R. L. Huguenin (1979), Mars surface composition from reflectance spectroscopy: A summary, *J. Geophys. Res., 84,* 8415–8426.

Smith, D., G. Neumann, R. E. Arvidson, E. A. Guinness, and S. Slavney (2003), Mars Global Surveyor Laser Altimeter Mission Experiment gridded data record, *MGS-M-MOLA-5-MEGDR-L3-V1.0,* NASA Planetary Data System, Washington Univ., St. Louis, Mo.

Squyres, S. W., and L. G. Evans (1992), Effects of material mixing on planetary gamma-ray spectroscopy, *J. Geophys. Res., 97,* 14,701–14,715.

Squyres, S. W., et al. (2004), In situ evidence for an ancient aqueous environment at Meridiani Planum, Mars, *Science, 306,* 1709–1714.

Surkov, Y. A., L. P. Moskaleva, V. P. Kharyukova, O. S. Manvelyan, and A. Golovin (1993), Gamma ray spectroscopy of Mars, in *Remote Geochemical Analysis: Elemental and Mineralogical Composition,* edited by C. M. Pieters and P. A. J. Englert, pp. 413–425, Cambridge Univ. Press, New York.

Tanaka, K. L., J. A. Skinner Jr., and T. M. Hare (2005), Geologic map of the northern plains of Mars, *Map SIM-2888,* scale 1:15,000,000, U.S. Geol. Surv., Boulder, Colo.

Taylor, G. J., et al. (2006a), Variations in K/Th on Mars, *J. Geophys. Res., 111,* E03S06, doi:10.1029/2006JE002676.

Taylor, G. J., et al. (2006b), Bulk composition and early differentiation of Mars, *J. Geophys. Res., 111,* E03S10, doi:10.1029/2005JE002645.

Taylor, J., et al. (2007), A global look at the composition of the Martian surface, *Eos Trans. AGU, 88*(23), Jt. Assem. Suppl., Abstract P41A-07.

Toulmin, P., III, A. K. Baird, B. C. Clark, K. Keil, H. J. Rose Jr., P. Christian, P. H. Evans, and W. C. Kelliher (1977), Geochemical and mineralogical interpretation of the Viking inorganic chemical results, *J. Geophys. Res., 82,* 4625–4634.

Trombka, J. I., et al. (1992), Analysis of Phobos gamma-ray spectra from the Phobos mission at Mars, *Proc. Lunar Planet. Sci. Conf., 22nd,* 23–29.

Trombka, J. I., et al. (2000), The elemental composition of asteroid 433 Eros: Results of the NEAR-Shoemaker X-ray Spectrometer, *Science, 289,* 2101–2105.

Wänke, H., J. Brückner, G. Dreibus, R. Rieder, and I. Ryabchikov (2001), Chemical composition of rocks and soils at the Pathfinder site, *Space Sci. Rev., 96,* 317–330.

Wyatt, M. B., and H. Y. McSween (2002), Spectral evidence for weathered basalt as an alternative to andesite in the northern lowlands of Mars, *Nature, 417,* 263–266.

Yen, A. S., et al. (2005), An integrated view of the chemistry and mineralogy of Martian soils, *Nature, 436,* 49–54.

Zimbelman, J. R., D. A. Crown, J. A. Grant, and D. M. Hooper (1997), The Medusae Fossae formation, Amazonis Planitia, Mars: Evaluation of proposed hypotheses of origin, *Lunar Planet. Sci., 28,* abstract 1482.

————————————

J. R. Arnold, Department of Chemistry, University of California, San Diego, La Jolla, CA 92093, USA. (jarnold@ucsd.edu)

V. Baker and J. M. Dohm, Department of Hydrology and Water Resources, University of Arizona, Tucson, AZ 85721, USA. (baker@hwr.arizona.edu; jmd@hwr.arizona.edu)

W. V. Boynton, M. K. Crombie, D. K. Hamara, D. M. Janes, K. E. Kerry, K. J. Kim, A. L. Sprague, and R. M. S. Williams, Lunar and Planetary Laboratory, University of Arizona, 1629 East University Boulevard, Tucson, AZ 85721, USA. (wboynton@lpl.arizona.edu; mkcrombi@lpl.arizona.edu; buck@gamma1.lpl.arizona.edu; daveh@lpl.arizona.edu; krisk@lpl.arizona.edu; kkim@lpl.arizona.edu; sprague@lpl.arizona.edu; remo@lpl.arizona.edu)

J. Brückner and H. Wänke, Max-Planck-Institut für Chemie, D-55128 Mainz, Germany. (brueckner@mpch-mainz.mpg.de; waenke@mpch-mainz.mpg.de)

D. M. Drake, TechSource, 1418 Luisa Street, Suite 1, Santa Fe, NM 87505, USA. (ddrake@mail.cybermesa.com)

L. d'Uston and O. Gasnault, Centre d'Etude Spatiale des Rayonnements, CNRS/UPS, F-31028 Toulouse, France. (lionel.duston@cesr.fr; olivier.gasnault@cesr.fr)

P. A. J. Englert and G. J. Taylor, Institute of Geophysics and Planetology, University of Hawaii at Manoa, Honolulu, HI 96822, USA. (penglert@hawaii.edu; gjtaylor@higp.hawaii.edu)

L. G. Evans, Science Programs, Computer Sciences Corporation, 7700 Hubble Drive, Lanham, MD 20706, USA. (larry.evans@gsfc.nasa.gov)

S. Karunatillake and S. W. Squyres, Center for Radiophysics and Space Research, Cornell University, Ithaca, NY 14853, USA. (wk43@cornell.edu; squyres@astrosun2.astro.cornell.edu)

J. M. Keller, Physics Department, California Polytechnic State University, San Luis Obispo, San Luis Obispo, CA 93407, USA. (jmkeller@calpoly.edu)

A. E. Metzger, Jet Propulsion Laboratory, California Institute of Technology, Pasadena, CA 91109, USA. (albert.e.metzger@jpl.nasa.gov)

I. Mitrofanov, Space Research Institute (IKI), 84/32 Profsoyuznaya Str., Moscow, Russia 117997. (imitrofa@iki.rssi.ru)

H. E. Newsom and R. C. Reedy, Institute of Meteoritics, University of New Mexico, Albuquerque, NM 87131, USA. (newsom@unm.edu; rreedy@unm.edu)

R. Starr, Department of Physics, Catholic University of America, Washington, D. C. 20064, USA. (richard.starr@gsfc.nasa.gov)

S. J. I. Trombka, NASA Goddard Space Flight Center, Greenbelt, MD 20771, USA. (jacob.i.trombka@nasa.gov)